

# WAVELET ANALYSIS OF WAVE MOTION

F. C. G. A. NICOLLEAU\*  
*SFMG, Department of Mechanical Engineering,  
The University of Sheffield,  
Mappin Street S1 3JD Sheffield, UK*

J. C. VASSILICOS  
*Department of Aeronautics, Imperial College of Science, Technology and Medicine,  
Prince Consort Road, South Kensington, London SW7 2BY, UK*

In this paper high resolution wave probe records are examined using wavelet techniques with a view to determining the sources and relative contributions of capillary wave energy along representative wind wave forms. Wavelets enable computations of conditional spectra and turn out to be powerful tools for the study of the development and propagation of capillary waves. They also enable the detailed analyses of the relative contributions to the spectrum of the wave peaks and troughs.

PACS numbers:  
Keywords:

## I. INTRODUCTION

The generation and dissipation of waves on the surface of the ocean under the influence of wind is a complicated process which has been investigated intensively over many years. With the advent of remote sensing techniques based on microwave backscatter from the ocean surface, particular interest has surrounded the microscale of those surface waves with wavelengths less than approximately 0.5 m. In the meantime wavelet methods have been developed and are now applied to a wide range of problems see e.g. [[11]]. Recent years have seen the development of Continuous Wavelet Transform (CWT), filter and threshold techniques, (which corresponds to the topic of this paper) details can be found in the review paper by [5]. There are also other applications of wavelets as reconstruction tools for synthetic turbulence methods (STM) (see for example the work of [12]). The study of wavelet energy spectrum for two-dimensional turbulence can also be found in [[10]].

In this contribution we report investigations of the structure of wind-forced microscale waves as elucidated by wavelet techniques. In particular, we focus on the behaviour of small scale capillary waves (with wavelengths less than approximately 20 mm) in relation to the larger scale gravity forms. Data used in this paper are tank waves measured by [2]. A small part of this  $2^{18}$  point long set of data is shown in figure 1 where the displacement of the wave  $h(t)$  is the quantity measured as a function of time  $t$ , the fetch  $d_f$  is 4.35 m and the wind speed  $u_w$  is  $48 \text{ m s}^{-1}$ . In §II we introduce general definitions and results about wavelets. In §III we compare wavelet and Fourier spectra of the tank waves and detail the respective contributions to the spectrum of the signal's peaks and troughs. In §IV we define conditional spectra which we use to achieve a better understanding of capillary waves. Finally in §V we compare our results to a fractal distribution of  $\Lambda$ -crest.

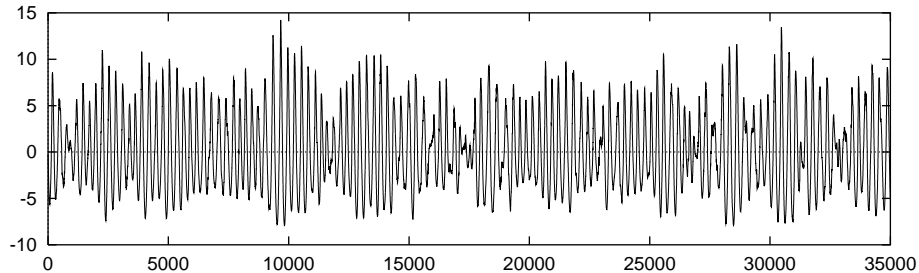


FIG. 1: Part of the signal analysed in this paper

The height  $h(t)$  in mm as a function of time  $t$  in ms, the fetch  $d_f$  is 4.35 m and the wind speed  $u_w$  is  $48 \text{ ms}^{-1}$ .

---

\* Corresponding author.

## II. MATHEMATICAL BACKGROUND AND DEFINITIONS

### A. The Wavelet transform

A wavelet transform of the function  $h(t)$  is defined as follows

$$\tilde{h}(t, \tau) = \tau^{-1} \int h(t') \psi^* \left( \frac{t' - t}{\tau} \right) dt', \quad (1)$$

where  $\psi(t)$  is the mother wavelet, \* indicates conjugate value,  $\tilde{h}$  is a function of two variables  $t$  and  $\tau$ ,  $t$  is the position in the physical space (here time),  $\tau$  the wavelet scale (here it is a scale of time that is a time lag or period).

The wavelet transform of  $h(t)$  can be expressed as a function of its Fourier transform [13]  $\hat{h}(\omega) = \int h(t) e^{-i\omega \cdot t} dt$  and the Fourier transform  $\hat{\psi}(\omega) = \int \psi(t) e^{-i\omega \cdot t} dt$  of  $\psi$  as follows:

$$\tilde{h}(t, \tau) = \tau^{-1} \int \hat{h}(\omega) \hat{\psi}(\tau\omega) e^{i\omega \cdot \tau} d\omega. \quad (2)$$

$\omega$  is the frequency that is the Fourier space variable corresponding to the time  $t$  in the real space. Figure 2 shows a smaller sample of the signal studied in this paper (upper frame), the ordinate is the height of the water level ( $h(t)$ ) and it is measured as a function of time which we refer to as the physical space ( $t$ ) throughout this paper. The

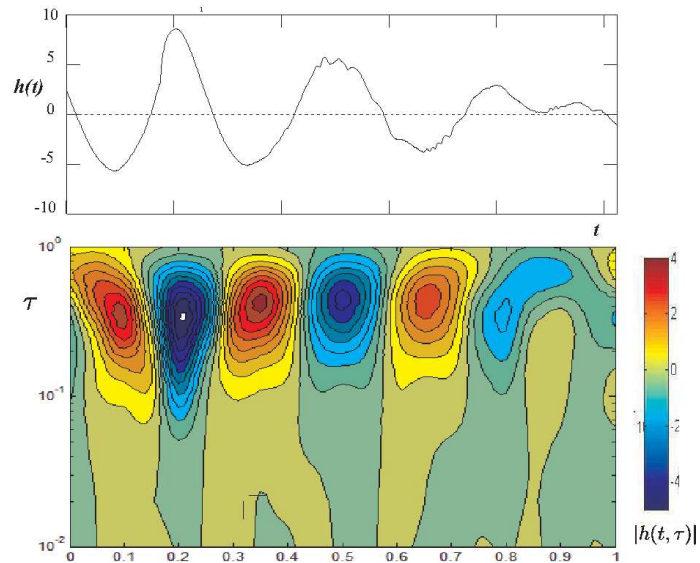


FIG. 2: Wavelet analysis of the 1024 first points of the wave signal in figure 1

Upper plot is the displacement  $h(t)$  in mm as a function of time  $t$  in ms, lower plot is its wavelet transform (same as figure 3 but viewed from a different angle). In this latter, the scale  $\tau$  is the ordinate and the time  $t$  the abscissa, curves represent iso-values of the wavelet transform modulus  $|\tilde{h}(t, \tau)|$ . The mother-wavelet is the Mexican-hat.

lower frame shows its wavelet transform, the ordinate axis holds the wavelet scale  $\tau$  and abscissa axis  $t$  the physical parameter. As shown in figure 3, the wavelet transform  $\tilde{h}(t, \tau)$  should be drawn along a third axis (upper plot), but in order to avoid complex 3-dimensional plots we opt for the drawing of  $\tilde{h}(t, \tau)$  iso-value curves in the  $(t, \tau)$  plane, that is curves defined as  $|\tilde{h}(t, \tau)| = cst$ . In practice, in this paper two mother-wavelets are used: the Mexican-hat wavelet (see appendix A) defined as

$$\psi(t) = \frac{d^2}{dt^2} e^{-\frac{1}{2}t^2} \quad (3)$$

and the Morlet wavelet (see B) defined as

$$\psi(t) = e^{-\frac{1}{2}t^2} e^{it}. \quad (4)$$

Both wavelets are based on the  $e^{-\frac{1}{2}t^2}$  shape, the Morlet-wavelet introducing a phase in the complex space. This Gaussian-type shape is quite close to the actual shape of an isolated tank wave. This is clear when comparing Figures 9 and 10 to the Mexican-hat mother-wavelet given in Figure 17, so we use this latter in particular to emphasize capillary and indentation effects in sections IV C and IV D. The merit of each wavelet is discussed later on and in the appendices.

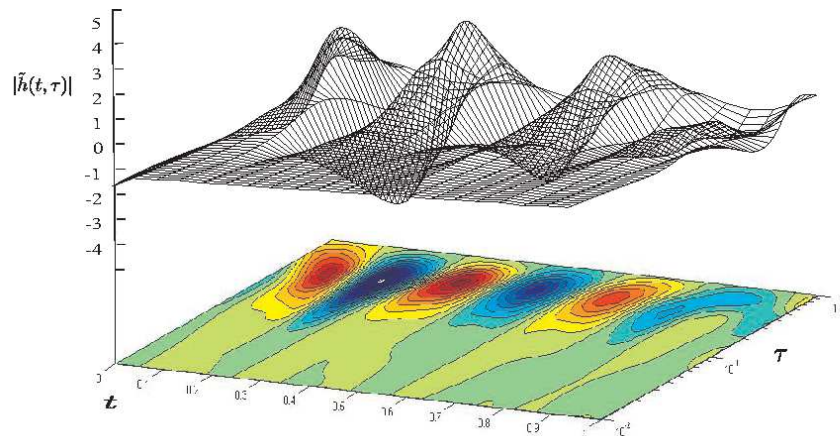


FIG. 3: Wavelet transform of signal in figure 2

Upper plot: Mexican-hat wavelet transform, lower plot: projection of the iso-value curves.

### B. Filtering

Wavelet transforms enable scale-filtering of signals. It is possible to inverse the wavelet transformation and reconstruct the signal. This inverse wavelet transformation is possible only when the mother wavelet verifies some properties of integrability, in particular that  $\int \psi(t)dt = 0$  (see [4]); wavelets used in this paper verify the required properties). The original signal can be expressed as a linear combination of its wavelet transform coefficients; the expression for this inversion is

$$h(t) = \int \int \tilde{h}(t', \tau) \frac{dt' d\tau}{\tau^2}. \quad (5)$$

Discarding certain scales in this reconstruction process defines a scale-filter. Such a filtering is particularly interesting for our data as it clearly appears that they contain at least two different ranges of scales (see section 3 and beyond):

- i) the main gravity wave scale,
- ii) the capillary waves and small scale indentations.

As we will see in §IV the wavelet-scales involved in the main gravity waves are clearly an order of magnitude or two larger than those involved in the capillarity effects and small-scales indentations. We propose to define the small-scales filtered signal  $h_{T_B}(t)$  as follows:

$$h_{T_B}(t) = \tilde{h}(t, T_B) \quad (6)$$

This is equivalent to using the filter  $\tau^2 \delta(\tau - T_B) \delta(t' - t)$  in the integration of the right hand side of (5). Figure 4 shows a portion of the signal  $h(t)$  in figure 1 and  $h_{T_B}(t)$  the result of the filtering out of scales smaller and larger than  $T_B$ .

### C. Local spectrum

From the wavelet transform of  $h(t)$  we can compute the local energy density [[4]]

$$\tilde{E}(t, \tau) = |\tilde{h}(t, \tau)|^2 \tau^2. \quad (7)$$

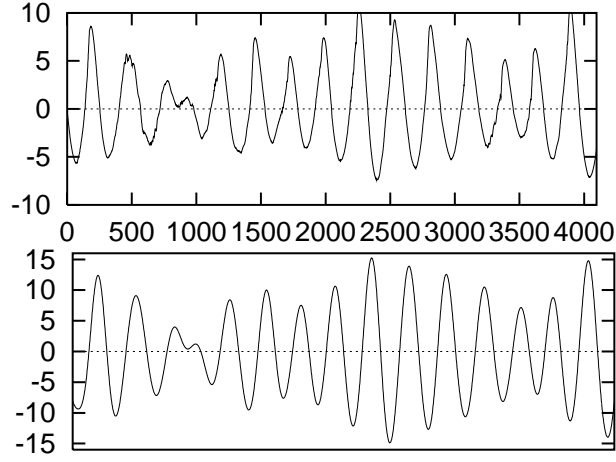


FIG. 4: Example of filtered signal

Top, the 4096 first points of the signal in figure 1, bottom the scale-filtering for a scale  $T_B = 0.4$ .

Equation (7) gives information about energy density associated with scale  $\tau$  and localised at time  $t$ . The global wavelet spectrum  $\tilde{E}(\tau)$  is the sum of all these local wavelet spectra,

$$\tilde{E}(\tau) = \int \tilde{E}(t, \tau) dt. \quad (8)$$

It relates to the Fourier spectrum:

$$\tilde{E}(\tau) = \int \left| \int \hat{h}(\omega) \hat{\psi}(\tau\omega) e^{i\omega t} d\omega \right|^2 dt.$$

With superscript \* indicating conjugate value,

$$\tilde{E}(\tau) = \int \int \int \hat{h}(\omega) \hat{\psi}(\tau\omega) \hat{h}^*(\omega') \hat{\psi}^*(\tau\omega') e^{i(\omega-\omega')t} d\omega d\omega' dt,$$

that is:

$$\tilde{E}(\tau) = \int \int \left\{ \int e^{i(\omega-\omega')t} dt \right\} \hat{h}(\omega) \hat{\psi}(\tau\omega) \hat{h}^*(\omega') \hat{\psi}^*(\tau\omega') d\omega d\omega',$$

$$\tilde{E}(\tau) = \int \int \delta(\omega - \omega') \hat{h}(\omega) \hat{h}^*(\omega') \hat{\psi}(\tau\omega) \hat{\psi}^*(\tau\omega') d\omega d\omega'$$

and eventually

$$\tilde{E}(\tau) = \int |\hat{h}(\omega)|^2 |\hat{\psi}(\tau\omega)|^2 d\omega. \quad (9)$$

The wavelet spectrum therefore appears as an average of Fourier spectra  $E(\omega) = |\hat{h}(\omega)|^2$  weighted with the wavelet term  $|\hat{\psi}(\tau\omega)|^2$ .

If the Fourier spectrum has a power law over a range of frequencies, i.e.  $E(\omega) \sim \omega^{-p}$  when  $\omega \rightarrow \infty$ , the change of variable  $k' = \tau\omega$  can be used to obtain the power law of  $\tilde{E}(\tau)$  when  $\tau \rightarrow 0$ . Indeed with this change of variables,

$$\tilde{E}(\tau) = 2\tau^{-1} \int E\left(\frac{k'}{\tau}\right) |\hat{\psi}(k')|^2 dk', \quad (10)$$

and in the limit  $\tau \rightarrow 0$  we have

$$\tilde{E}(\tau) = 2\tau^{p-1} \int k'^{-p} |\hat{\psi}(k')|^2 dk',$$

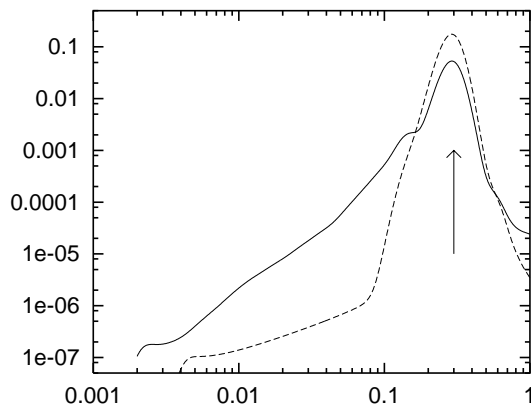


FIG. 5: Wavelet spectrum of a sample of the signal shown in figure 1  $\tilde{E}(\tau)$  using the Morlet wavelet for a 131072 point long data sample; solid line: entire signal, dash line: filtered signal  $h_{T_B}(t)$ .

that is:

$$\tilde{E}(\tau) \sim \tau^{p-1}. \quad (11)$$

This result is independent of the choice of the wavelet  $\psi$  but due to the fact that the integral in (10) is in practice taken over a finite range of  $k'$ , some wavelets give better results than others. We use here the Morlet wavelet to educe cut-off scales (see appendix B) and the Mexican-hat wavelet to educe power law spectra (see appendix A).

#### D. Conditional spectrum

The definition of the wavelet spectrum allows definitions of conditional spectra. A conditional spectrum is defined as the integration of the wavelet local spectrum over a given region ( $V_c$ ) in the physical space where the required condition is met.

$$\tilde{E}_c(\tau) = \frac{1}{V_c} \int_{V_c} \tilde{E}(t, \tau) dt. \quad (12)$$

In our case of analysing tank waves, we can define different conditions to educe the contribution of the peaks, troughs and different parts of the elementary waves to the global spectrum. The variation of  $\tilde{E}_c(\tau)$  according to the definition of  $V_c$  gives information on how the global spectrum relates to the different regions in the physical space. For instance contribution to the spectrum of peaks in the data can be estimated by setting the condition

$$h(t) > \epsilon, \quad (13)$$

as in §III-III C. The higher the value of  $\epsilon$  the more affected is the conditional spectrum by the peaks. Similarly, the condition

$$h(t) < \epsilon \quad (14)$$

gives information on how the global spectrum relates to the trough regions as in §III-III D. It is also possible to condition the spectrum on different parts of each elementary wave as shown in §IV.

### III. SPECTRUM OF THE TANK WAVES

#### A. Wavelet spectrum

Figure 5 shows the wavelet spectrum  $\tilde{E}(\tau)$  of the displacement  $h(t)$  as a function of the scale  $\tau$ . Solid lines correspond to the entire 131072 point long data sample of the signal shown in figure 1 and dash lines to the same signal  $h_{T_B}(\tau)$  filtered at the scale  $T_B = 0.4$ . Note how the Morlet wavelet spectrum can be used to educe characteristic frequencies,

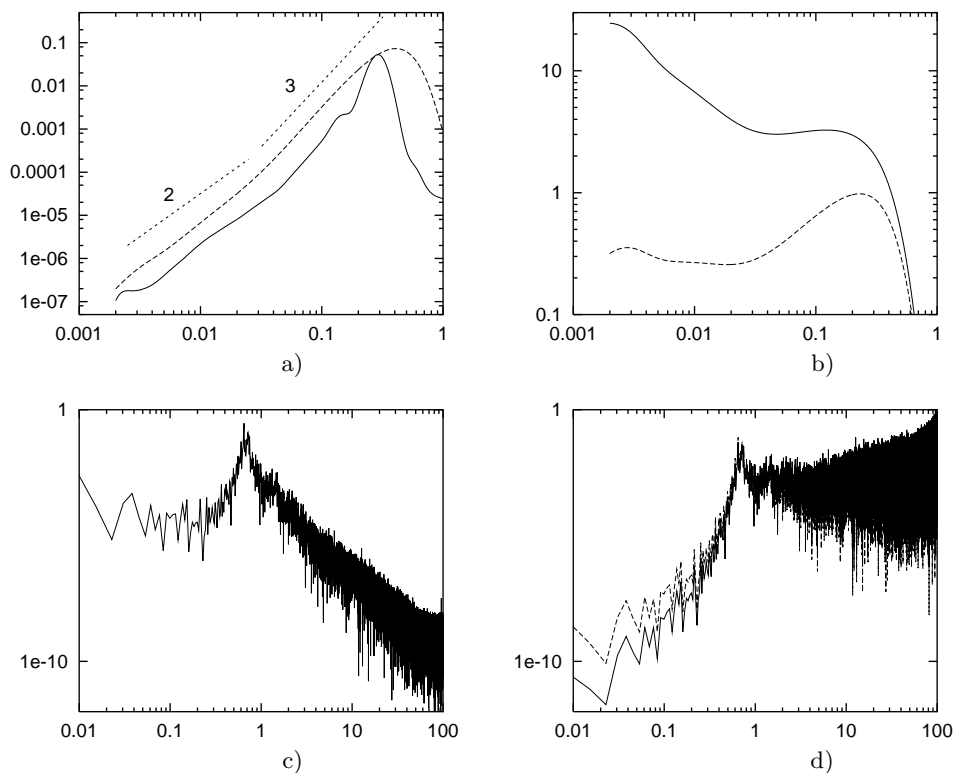


FIG. 6: Wavelet and Fourier spectra of a 131072 point long data sample of the signal shown in figure 1  
a) Wavelet spectra  $\tilde{E}(\tau)$  as a function of  $\tau$  for Mexican-hat (upper curve) and Morlet wavelet (lower curve). b)  $\tau^3 \tilde{E}(\tau)$  (upper curve) and  $\tau^{2.3} \tilde{E}(\tau)$  (lower curve) as functions of  $\tau$  for the spectrum based on the Mexican-hat wavelet. c) Fourier spectrum  $E(\omega)$  as a function of  $\omega$  for the same data sample. d)  $\omega^4 E(\omega)$  as a function of  $\omega$  (upper curve) and  $\omega^3 E(\omega)$  -  $\omega \approx \frac{2\pi}{\tau}$ .

which can of course also be done by Fourier methods. The filtered signal has virtually no wavelet intensity at small scales. All the wavelet intensity is focused on the scale 0.3 corresponding to the distance  $2\lambda$  between two minima or two maxima of the signal. Direct measurement of the average value of  $\lambda$  over the entire signal gives  $\lambda \approx 0.13$ . Filtering the signal does not alter the position of its zero-crossings but it drastically changes the shapes of the waves mainly by smoothing them and making them more top-bottom symmetric. (see figure 4). Hence one can conclude from figure 5 that the small- $\tau$  part of the wavelet spectrum ( $\tau < 0.13$ ) is mainly due to the shape of each individual wave, a fact confirmed by the analysis of an isolated wave in §IV.

Figures 6a,b show the wavelet spectrum  $\tilde{E}(\tau)$  of the signal in figure 1 based on the Mexican-hat wavelet which is suitable for educing power laws. It is not possible to conclude on the existence of power laws for these data, the range of scales being very small, but it is possible to educe two different regions. Asymptotically for  $\tau$  small we seem to have  $\tilde{E}(\tau) \sim \tau^{2.3}$  (see figure 6b) in the range  $\tau_c < \tau < \tau_{trans}$  where  $\tau_c = 0.002$  is the lower cut-off scale of the data[14] and  $\tau_{trans}$  the upper limit for this first region (here  $\tau_{trans} \sim 0.03$ ). For larger scales ( $\tau > \tau_{trans}$ ) we seem to have  $\tilde{E}(\tau) \sim \tau^3$  (see figure 6b), which according to (11) corresponds to a Fourier spectrum  $E(\omega) \sim \omega^{-4}$ , a result consistent with the existence of  $\Lambda$ -crests (that is crests with discontinuity in slope) all of same duration. In §IIIIII B we show that the accuracy on  $\tilde{E}(\tau)$  is by far superior to that on  $E(\omega)$ .

## B. Comparison with Fourier spectrum analysis

The Fourier spectrum of  $h(t)$  is classically defined as

$$E(\omega) = |\hat{h}(\omega)|^2. \quad (15)$$

The Fourier spectrum of the signal in figure 1 is given in figure 6c. It contains a lot of noise which is not the case of the wavelet spectra curves  $\tilde{E}(\tau)$  (figure 6a). The peak is reached at  $\omega = 13.5$ , that is  $\tau = 2\pi/\omega = 0.465$ , and a slope may be observed in the range 15–300. Figure 6d shows both  $\omega^4 E(\omega)$  and  $\omega^3 E(\omega)$ . Due to the noise it is difficult to

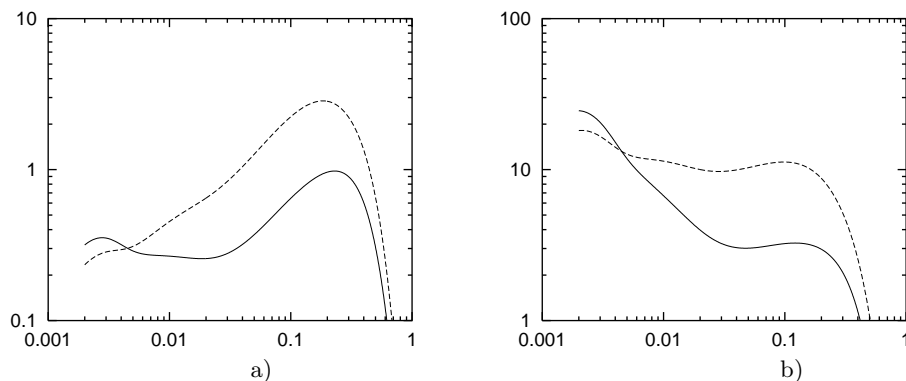


FIG. 7: Conditional spectra based on the condition  $h(t) > \epsilon$

From the signal in figure 1, power spectra are based on 131072 points and we use the Mexican-hat wavelet. a)  $\tau^{-2.3}\tilde{E}_c(\tau)$  against  $\tau$  for the entire signal (lower curve) and for  $\epsilon = 5$ , b)  $\tau^{-3}\tilde{E}_c(\tau)$  against  $\tau$  for the entire signal (lower curve) and for  $\epsilon = 5$ .

decide whether  $E(\omega) \sim \omega^{-4}$  or  $E(\omega) \sim \omega^{-3}$ . It seems however that  $E(\omega) \sim \omega^{-4}$  in the range 15–300 and  $E(\omega) \sim \omega^{-3}$  in the range 300–1000. We show in section 4 that this value of  $\omega \sim 300$  or  $\tau \sim 0.003$  is rather close to the scale ( $\sim 0.010$ ) of very small perturbations observed on certain parts of the signal.

### C. Energy spectrum of peaks in the signal

In this section, condition (13) is used to compute conditional spectra for the 131072 first points of the signal in figure 1. Figure 7a shows the compensated non conditioned spectrum  $\tau^{-2.3}\tilde{E}(\tau)$  (lower curve) and the compensated conditional spectrum (upper curve) based on the criterion  $h(t) > 5$ . This latter spectrum is associated with peaks: from figure 1, one can see that for  $\epsilon \geq 5$ , the conditioned signal is just a sum of isolated wave-crests. It is clear from figure 7a that peaks play no part in the power law  $\tilde{E}(\tau) \sim \tau^{2.3}$  observed for the small scales (i.e.  $\tau < \tau_{trans}$ ) in the non conditioned signal. Figure 7b shows the compensated spectrum  $\tau^{-3}\tilde{E}(\tau)$  obtained from the entire signal and from the condition  $h(t) > 5$ . The conditional spectrum is closer to  $\tilde{E}(\tau) \sim \tau^3$  down to small scales  $\tau < \tau_{trans}$ . A transition still appears at the scale  $\tau = \tau_{trans}$  but it is much less stressed than in the case of the entire signal.

From this spectral analysis we can conclude that the signal's peaks are close to discontinuities in slope. Indeed, it is known from Fourier analysis that such discontinuities are characterised by a  $\omega^{-4}$  spectrum. This indicates that for  $\tau > \tau_{trans}$ , the signal's spectrum is dominated by wave-crests. (See §IVIV A for the analysis of an isolated crest.)

### D. Energy spectrum of the troughs in the signal

Using condition (14) we now analyse the local spectrum of the troughs. The conditional wavelet spectra shown in figure 8 give some idea of the shape of the local spectrum associated with troughs. Again there are two ranges of scales  $\tau$  separated by a value  $\tau_{trans}$ , and the lower  $\epsilon$  - i.e. the closer to the troughs - the smaller  $\tau_{trans}$ . Figure 8b shows the compensated spectra  $\tau^\alpha\tilde{E}(\tau)$ . It seems that troughs do not have a  $\tau^3$  wavelet spectrum but are closer to a  $\tau^4$  power law in the range  $\tau_{trans} < \tau < 0.2$ . Trough and peak regions have different contributions to the global energy spectrum.

## IV. CAPILLARY EFFECTS

### A. Analysis of an isolated wave

We can limit our study to an isolated wave such as the one in figure 9a. A common feature of water waves is the small scale parasitic capillary waves which are present on the forward faces. Water waves with lengths less than about 10mm are called capillary waves and those riding on the forward faces of the larger gravity forms are called parasitic capillaries because they derive their energy from the larger wave. These capillary waves are clearly deduced with the use of wavelet transform as can be seen in figure 9b. The wavelet transform clearly localises a main discontinuity at

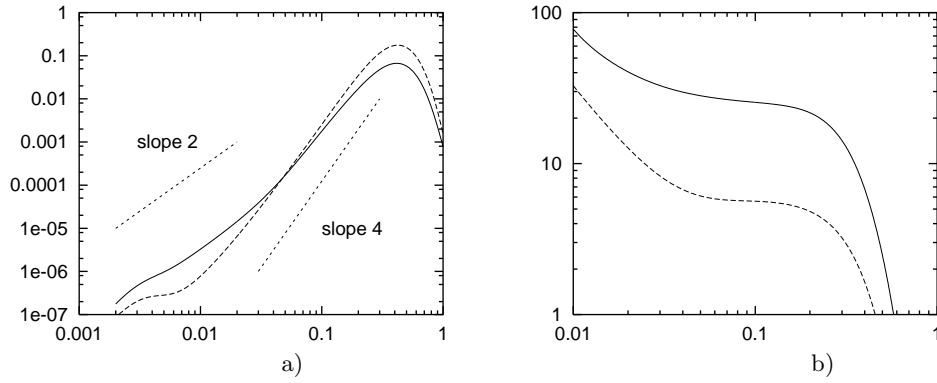


FIG. 8:  $\tilde{E}(\tau)$ , spectra conditioned on the troughs:  $h(t) < \epsilon$

For  $\epsilon = 0$  solid line and  $\epsilon = -5$  dash line, a) wavelet spectrum, b)  $\tau^{-3.5}\tilde{E}(\tau)$  for the spectrum conditioned on  $h(t) < 0$  (solid line) and  $\tau^{-4}\tilde{E}(\tau)$  for the spectrum conditioned on  $h(t) < -5$  (dash line), spectra are measured on a  $2^{17}$  point long sample and based on the Mexican-hat wavelet.

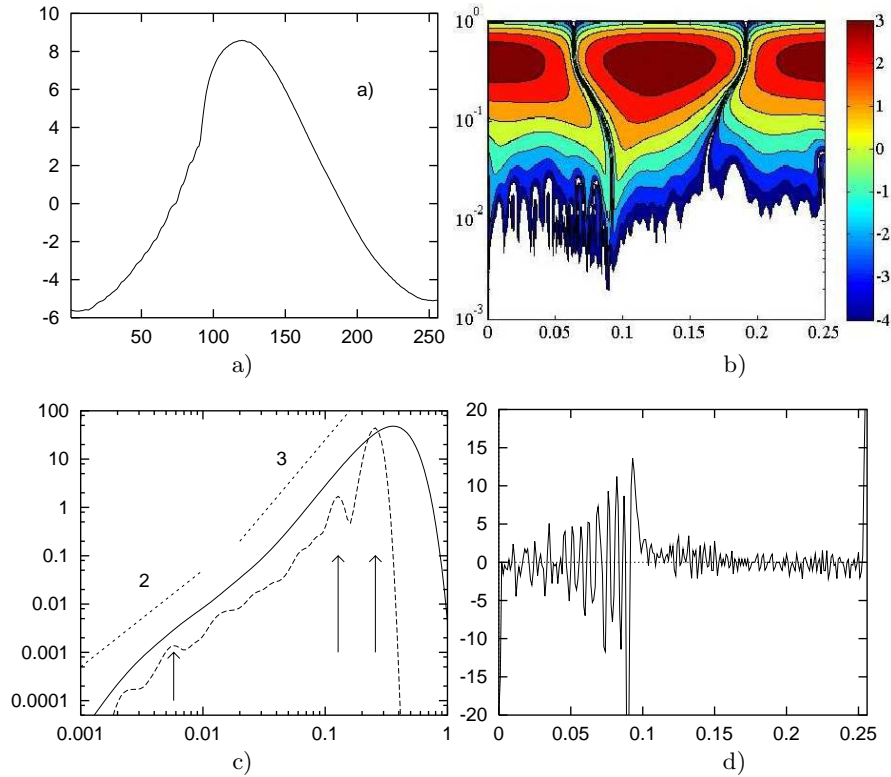


FIG. 9: Isolated wave, 256 points

a) Displacement  $h(t)$  measured as a function of  $t$  given in milliseconds. b) Wavelet transform of the displacement, plot in semi-log, the y-axis holds the scale parameter  $\tau$  and the x-axis holds the physical parameter  $t$  given in seconds. Curves are iso-values of the wavelet energy  $|\tilde{h}(t, \tau)| = cst$ . c) Wavelet spectra based on Mexican-hat (solid line) and Morlet (dashed line) wavelets. d)  $\tilde{h}(t, \tau = 0.005)$  using the Mexican-hat wavelet.

$t = 0.09 \pm 0.001$ . Capillary waves appear as blobs of wavelet intensity in the interval  $0 < t < 0.09$  (i.e. on the forward face), and they are associated with a characteristic period (scale  $\tau$ ) of the order of  $\tau \sim 0.01$ .

Figure 9c shows the wavelet spectra based on Mexican-hat (solid line) and Morlet (dashed line) wavelets for the signal in figure 9a. The Morlet wavelet is good at educing cut-off scales and the wave frequency. The wave period and half-period are shown by the arrows at 0.257 and 0.127, the third arrow points to the capillary wave period 0.0056. These values are consistent with an examination of figure 9b, i.e. the capillary wave period is 1/50 of the characteristic period of the larger scale gravity wave which appears as large scale blobs at the top of figure 9b. The Mexican-hat

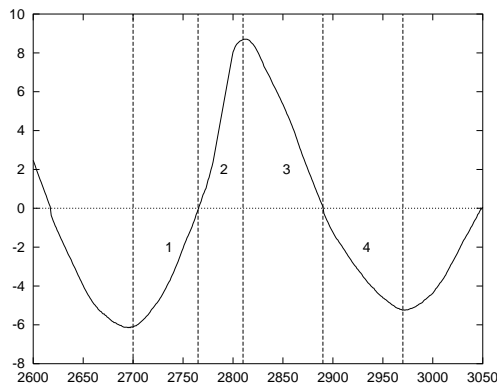


FIG. 10: Definition of the elementary parts of an isolated wave on an example of a wave different from figure 9

wavelet is clearly better at educing the spectral power law  $\tilde{E}(\tau) \sim \tau^p$ . Slopes 2 and 3 are drawn in figure 9c giving an indication of possible power laws but ranges are too small to conclude here.

The scale associated to the capillary effect being clearly educed, figure 9 shows the filtered the signal for this scale  $\tau = 0.005$ .

### B. Wavelet spectra conditioned on phases

It is also possible to condition the spectrum on the different part of each elementary wave as shown in figure 10. Wind blows from 4 to 1; four conditional spectra can be defined corresponding to each region 1,2,3,4 of the wave. The wave breaking occurs in region 2 and capillary effects are observed in region 1 and 4.

An especially important feature of our data is the propagation of capillary waves in the highly sheared current of the viscous boundary layer. Parasitic capillary waves are generated by small-scale gravity waves. Extensive theoretical and numerical investigations by [6] (see references there in) has revealed the mechanisms linking the formation of small scale gravity waves with the parasitic capillary waves located downwind of their crests. The combined effects of surface tension and high curvature at the crests of small gravity waves form a localised moving disturbance at the surface. This disturbance generates capillary waves upstream and gravity waves downstream due to the dispersion relation near the gravity/capillary transition.

The breaking of small scale gravity waves results in the generation of capillary waves. During the breaking process, wave energy is not only dissipated by subsurface turbulence but is also radiated from the breaking region [[9]]. The relationship between these generated waves and the underlying gravity wave form is probably most clearly revealed by the laboratory experiments of [Banner & Fooks 1985]. Notably, the frequencies of these waves are substantially higher than the gravity wave and the influence of capillarity makes these waves highly dissipative and, therefore, short lived. Their random formation and rapid dissipation makes monitoring their motion exceedingly difficult.

Uncertainty existed as to the direction of propagation of waves generated by breaking as it has been suggested that the wind drift at the crest was greatly intensified by local tangential stresses. Recent work by [2] has shown that relative to the moving wave form (except in the immediate vicinity of the spilling region) the mean wind drift is approximately  $0.3(\pm 0.1)u_*$  and transport is in an upwind direction. Whilst the sources of capillary wave energy have been identified, very few investigations have endeavoured to distinguish between their relative contributions to surface wave energy. In particular, the investigations of [Banner & Fooks 1985] have ignored the role of wind, yet the wind itself is plainly able to generate capillary ripples. Furthermore, the conclusions of these two detailed studies is that a strong relationship exists between the larger scale wave and the high frequency motions which occur on its surface. Yet the spectral relationships determined take no account of these directly.

Here, the high resolution wave probe record is examined using wavelet techniques with a view to determining the sources and relative contributions of capillary wave energy along representative wind wave forms. Figures 11 show comparisons of the entire spectrum, upper curves in each plot, with conditional spectra based on sector 1,2,3,4 defined in figure 10. Note that these spectra are obtained from the entire data set and not from individual waves such as figures 10 and 9a, thus providing conclusions on the average behaviour of sectors 1,2,3 and 4. These conclusions are:

i) figure 11b shows that the dominant contribution of small scale energy comes from sector 2, that is where the breaking of the wave occurs.

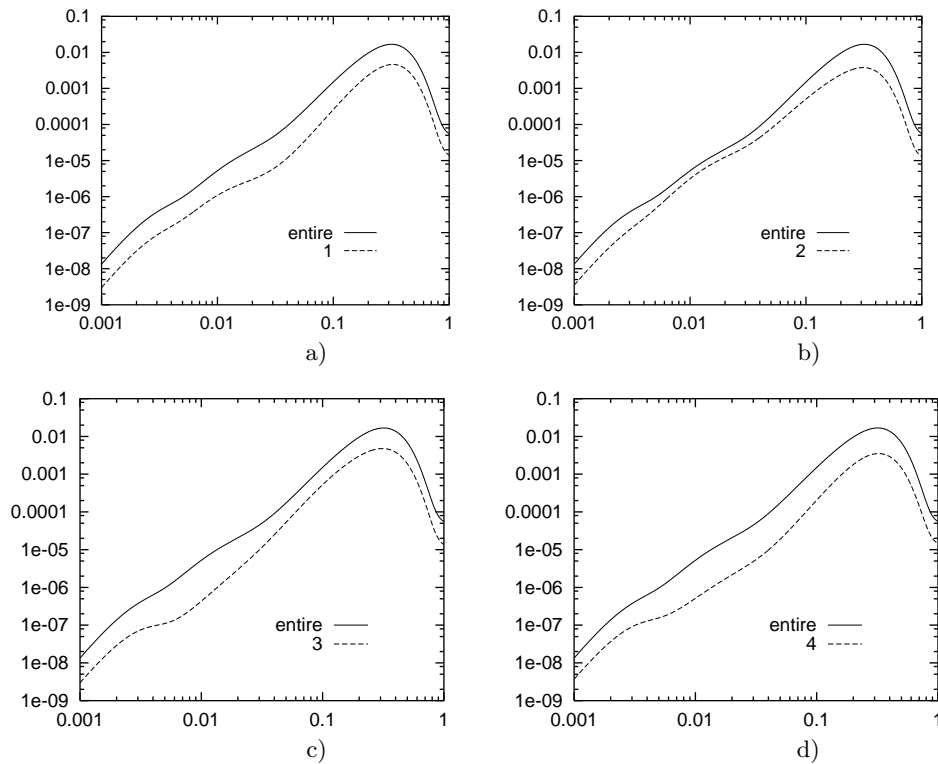


FIG. 11: Conditional spectra, 1,2,3,4 refer to conditions described in figure 10

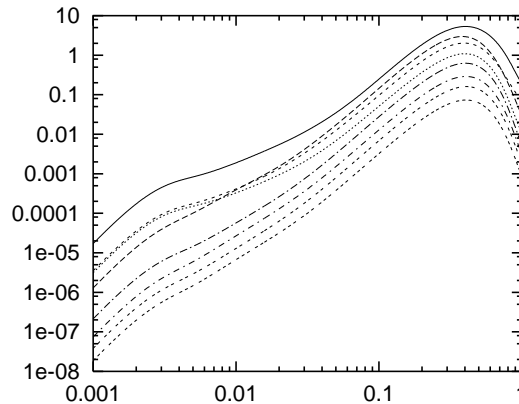


FIG. 12: Mexican-hat wavelet spectra for different length data samples  
From top to bottom  $2^{10}$ ,  $2^{11}$ ,  $2^{12}$ ,  $2^{13}$ ,  $2^{14}$ ,  $2^{15}$ ,  $2^{16}$ ,  $2^{17}$  point long segments.

ii) Sector 1 (figure 11a) shows higher levels of small scale energy than sector 3 (figure 11c) this is consistent with a major contribution from the parasitic capillaries developing in sector 1.

iii) Sector 3 shows higher levels of large scale energy than sector 1, this may be associated with the non-linearity of the waves in this part.

iv) Sector 4 (figure 11d) shows a slightly higher level of small scale energy than sector 3, indicating some capillary leakage towards the downwind crest.

These conclusions support the view that the direction of propagation of waves generated by breaking is from sector 2, to sector 1 to sector 4 of the subsequent wave with no indication that these waves exist in sector 3.

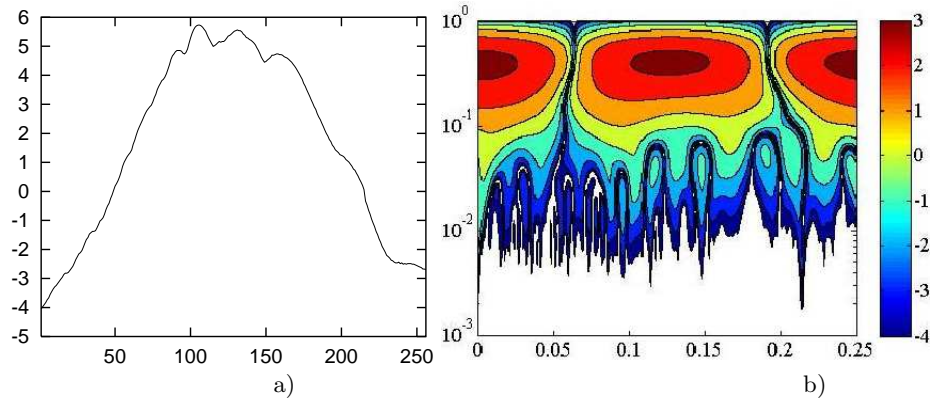


FIG. 13: Isolated wave with large indentations

a) 256 points long signal in milliseconds, b) wavelet transform of 13a, iso-value sampling is the same as in figure 9 and  $t$  and  $\tau$  are in seconds.

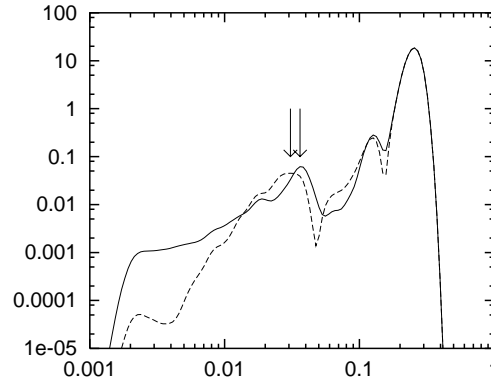


FIG. 14: Wavelet spectrum of the isolated wave in figure 13

Solid line wavelet spectrum of the entire wave, dashed line wavelet spectrum conditioned on  $h(t) > 5$ . Arrows indicate scales 0.031 and 0.036.

### C. The distribution of capillary wave periods

In the wavelet spectra shown in figure 11, samples larger than  $2^{17}$  have been used. One can see from these spectra that the capillary wave period disappears from the total energy spectrum based on  $2^{17}$  points. The sample length can be varied to get an idea of the breadth of the distribution of capillary wave periods at different scales. Figure 12 shows wavelet spectra corresponding to different sample sizes of the signal in figure 1. At small scales  $0.001 < \tau < 0.05$ , the shape of the spectrum needs samples longer than  $2^{14}$  points to converge, whereas the spectrum shape at large scales is not affected. This is an indication that the distribution of capillary wave periods is broader at small scales than at large ones.

### D. Large scale indentations:

We now focus on large scale indentations like those in figure 13a. These are indentations at scales larger than the capillary wave ones but still smaller than the large scale  $\lambda$  educed in §3(a). Figure 13b is a plot of the wavelet transform of the signal. A comparison of figures 9b and 13b shows that the wavelet-scales of the large scale indentations are clearly an order of magnitude smaller than  $\lambda$  and can be up to an order of magnitude larger than the wavelet scales involved in capillary effects. The scales associated with the large indentations in figure 13a are not localised on the forward face and lie between  $t=0.031$  s and 0.036 s. They are therefore clearly differentiated from the capillarity waves analysed in the previous section.

Figure 14 shows the wavelet spectrum and the conditional wavelet spectrum of signal in figure 13a. The conditional spectrum is closer to the  $\tilde{E}(\tau) \sim \tau^3$  law indicating that, contrary to capillary waves, the large indentations in figure 13a

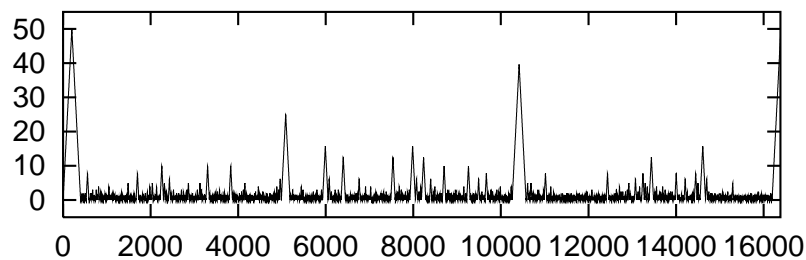


FIG. 15: Signal  $h(t)$  constructed as a sum of a fractal distribution of  $\Lambda$ -crests for  $D_1 = 0.5$ ,  $\lambda_{min} = 1$  and  $\lambda_{max} = 100$ .

may be closer to slope discontinuities, but the range is too short to enable a definitive conclusion.

## V. ANALYSIS OF A FRACTAL DISTRIBUTION OF $\lambda$

In this section we analyse a signal having a fractal distribution of  $\lambda$  (the distance between two consecutive zero-crossings), that is [[3]]:

$$M(\lambda) d\lambda = \frac{M_{max}}{\lambda_{max}} \left( \frac{\lambda_{max}}{\lambda} \right)^{D_1+1} d\lambda \quad (16)$$

where  $M(\lambda)$  is the number density of  $\Lambda$ -crests of size between  $\lambda$  and  $\lambda + d\lambda$  and we assume  $0 < D_1$  and  $\lambda < \lambda_{max}$ . This signal is constructed as a sum of  $\Lambda$ -crests which are exactly slope-discontinuities with the same angle between two slopes forming a discontinuity. Hence the signal is constructed as a fractal distribution of self-affine  $\Lambda$ -crests (see figure 15).

[3] have shown that the Fourier spectrum of such a 1-D signal follows the power law

$$E(\omega) \sim \frac{1}{\omega^4} (\omega \lambda_{max})^{D_1} \quad (17)$$

for  $\omega \lambda_{max} \gg 1$ . Using (11) we can deduce that

$$E(\tau) \sim \tau^{3-D_1} \quad (18)$$

for  $\frac{\tau}{\lambda_{max}} \ll 1$  and can also use wavelet spectra conditioned on  $h(t) > \epsilon$  to isolate  $\Lambda$ -crests and show that for  $\epsilon$  large enough

$$E_c(\tau) \sim \tau^3 \quad (19)$$

even though  $E(\tau) \sim \tau^{3-D_1}$  for  $\frac{\tau}{\lambda_{max}} \ll 1$ . Hence, wavelet methods can be used to show the existence of  $\omega^{-4+D_1}$  spectra but also to demonstrate, when the case may be, that these power-law spectra are related to  $\Lambda$ -crests which themselves have  $\omega^{-4}$  energy spectra.

Figure 16a is a log-log plot of  $\lambda_{max}M(\lambda)$  versus  $\lambda$  enabling direct verification of the fractal distribution of  $\lambda$  with  $D_1 = 0.5$ . Figure 16b is a plot of the wavelet spectrum of the signal in figure 15 (using the 131072 points of this signal) and it is based on the Morlet wavelet. The solid line corresponds to the entire signal, the dash line to the signal conditioned on  $h(t) > \epsilon > 10$ . We can draw the following conclusions:

i) there is no particular peak in these spectra as was the case in the experimental data studied in the previous sections. This is consistent with the notion of a fractal distribution which implies that there is no privileged scale.

ii) The spectrum of the entire data is dominated by the fractal distribution of the peaks: the law for the wavelet-spectrum is  $\tilde{E}(\tau) \sim \tau^{1.5}$  which yields a Fourier spectrum  $E(\omega) \sim \omega^{-2.5}$  in agreement with relations (17) and (18) for  $D_1 = 0.5$ .

iii) The spectrum associated with the  $\Lambda$ -crests is deduced by the conditioned spectrum based on the condition  $h(t) > 10$ . We find  $\tilde{E}_c(\tau) \sim \tau^3$  which agrees with relation (19) for slope discontinuities.

For the sake of completeness we should also mention the possibility of a fractal distribution of scales over a limited range which would generate a scale-dependent behaviour of the kind of the ‘parabolic scale invariance’ introduced in [[8]].

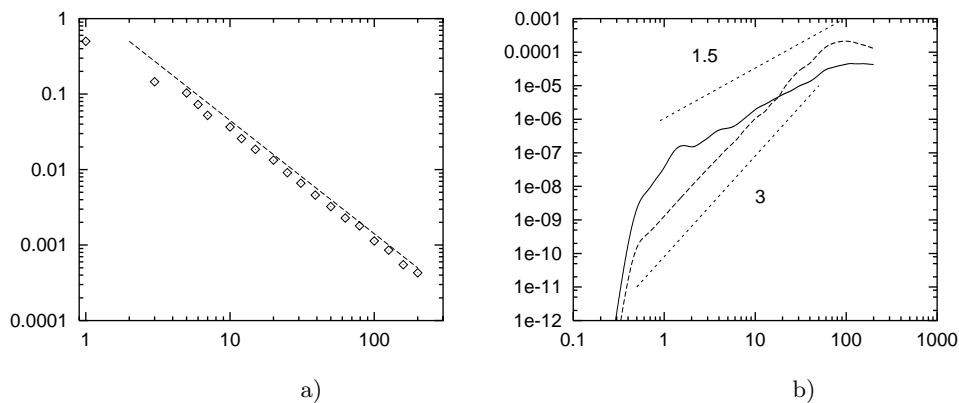


FIG. 16: Fractal and Wavelet analyses of signal shown in figure 15

a) Probability density function of  $\lambda_{max}M(\lambda)$  as a function of  $\lambda$  for the signal's first 300000 points. The straight line is the slope -1.5. b) Wavelet transform of the signal's first 131072 points based on the Morlet wavelet. The solid curve corresponds to the entire sample, the dash curve to the condition  $\epsilon > 10$ .

## VI. CONCLUSION

In this paper we have used conditional spectra based on wavelet decompositions to analyse time series of displacement of tank waves. We have shown that wavelets can educe capillary waves from the signal. Wavelet spectrum analysis has also enabled us to quantify the relative contribution of peaks and troughs to the energy spectrum. Wave peaks are close to slope discontinuities whereas wave troughs are not. Wavelet spectra conditioned on wave sectors show that capillary waves are mainly located in sector 1 with some capillary leakage downwind from the peak of the wave indicating that capillary waves propagate downwind.

The wavelet analysis we presented here was tuned to our particular application. There are many examples of forced microscale waves, for example the wave displacement in driven metal plates in [[7]]; though the turbulence there is classified as weak it is richer in scales than the case presented in this paper. Such cases would be interesting study cases as preliminary to the use of wavelet analysis to the study of fully developed turbulence.

### Acknowledgements

We are grateful to W. L. Peirson for enabling us to use his data. JCV acknowledges supports from the Royal Society.

### Appendix A: Mexican-hat wavelet

Wavelets based on the Gaussian function have the form:

$$\psi(t) = \frac{d^n}{dt^n} e^{-\frac{1}{2}t^2}, \quad (\text{A1})$$

the case  $n = 2$  corresponds to the Mexican-hat wavelet. Their Fourier transforms have the simple form:

$$\hat{\psi}(\omega) = (i\omega)^n e^{-\frac{1}{2}\omega^2}. \quad (\text{A2})$$

These wavelets are interesting for the study of the zero-crossings of signals but can be misleading in the study of spectrum power laws. Indeed, with these functions as mother wavelets, the wavelet spectrum asymptotic limit is

$$\lim_{\tau \rightarrow 0} \tilde{E}(\tau) \sim \tau^{2n},$$

whatever the Fourier spectrum. This is due to the fact that in practise a power law spectrum is not verified over an infinite range of scale but has an upper  $\omega_{max}$  and lower  $\omega_{min}$  cut-off scale. Using this remark and plugging (A2) into

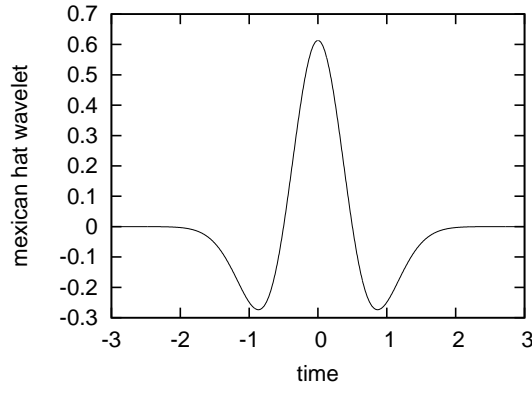


FIG. 17: Typical Mexican-hat wavelet.

the definition of the wavelet spectrum (9), it yields:

$$\tilde{E}(\tau) = \int_{\omega_{min}}^{\omega_{max}} |\hat{h}(\omega)|^2 (\tau\omega)^{2n} e^{-(\tau\omega)^2} d\omega,$$

that is

$$\tilde{E}(\tau) = \tau^{2n} \int_{\omega_{min}}^{\omega_{max}} |\hat{h}(\omega)|^2 \omega^{2n} e^{-(\tau\omega)^2} d\omega.$$

Because  $\omega_{min}$  and  $\omega_{max}$  are finite  $\tau$  can go to 0 while  $\omega$  is bounded, and

$$\lim_{\tau \rightarrow 0} e^{-(\tau\omega)^2} = 1$$

is valid outside the range  $\frac{1}{\omega_{max}} < \tau < \frac{1}{\omega_{min}}$ . Then

$$\tilde{E}(\tau) \sim \tau^{2n} \int_{\omega_{min}}^{\omega_{max}} |\hat{h}(\omega)|^2 \omega^{2n} d\omega,$$

that is

$$\tilde{E}(\tau) \sim \tau^{2n}$$

whatever the form of  $|\hat{h}(\omega)|^2$ . This asymptotic behaviour proper to the wavelet can parasite the spectrum power law we are looking for. Figure 18 shows the wavelet spectrum form 3 wavelets:  $\frac{d^2}{dt^2} e^{-\frac{1}{2}t^2}$ ,  $\frac{d^4}{dt^4} e^{-\frac{1}{2}t^2}$  and the Morlet wavelet (see § B).

### Appendix B: Morlet wavelet

The Morlet wavelet is defined as:

$$\psi(t) = e^{-\frac{1}{2}t^2} e^{it}. \quad (\text{B1})$$

and its Fourier transform is  $\hat{\psi}(\omega) = e^{-\frac{1}{2}(\omega-\omega_0)^2}$ . If we use this wavelet in the computation of (9) then

$$\tilde{E}(\tau) \sim \int_{\omega_{min}}^{\omega_{max}} |\hat{h}(\omega)|^2 d\omega \quad (\text{B2})$$

when  $\tau \rightarrow 0$  and there is no asymptotic power law introduced in that limit. when  $\tau \rightarrow 0$ . On the other hand due to its cosine-like form, Morlet wavelet tends to focus on a scale when it is periodic at the expense of the resolution of the power spectrum (where it exists). As it appears in figure 18 apart from the determination of cut-off scales, the Mexican-hat wavelet is more appropriate for the determination of the power law of a spectrum.

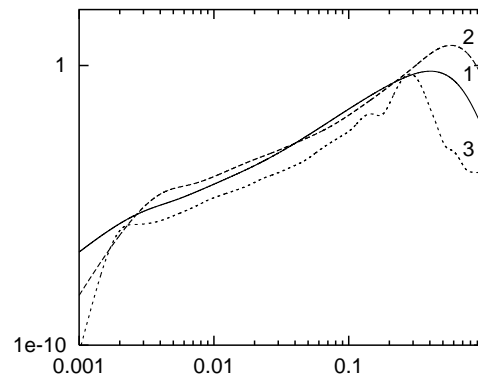


FIG. 18:  $\tilde{E}(\tau)$  as a function of  $\tau$  for 3 different wavelets  
 1)  $\frac{d^2}{dt^2}e^{-\frac{1}{2}t^2}$ , 2)  $\frac{d^4}{dt^4}e^{-\frac{1}{2}t^2}$ , 3) Morlet wavelet. the cut-off is the clearer with the Morlet wavelet.

*Journal reference:*

- [Banner & Fooks 1985] BANNER, M. L. & FOOKS, E. H. 1985 On the microwave reflectivity of small-scale breaking water waves. *Proc. Roy. Soc. Lond. A* **399** (1816), 93–109.
- [2] BANNER, M. L. & PEIRSON, W. L. 1998 Tangential stress beneath wind-driven air-water interfaces. *J. Fluid Mech.* **364**, 115–145.
- [3] BELCHER, S. E. & VASSILICOS, J. C. 1997 Breaking waves and the equilibrium range of wind wave spectra. *J. Fluid Mech.* **342**, 377–401.
- [4] FARGE, M. 1992 Wavelet transforms and their applications to turbulence. *Annu. Rev. of Fluid Mech.* **24**, 395–457.
- [5] M. Farge, R. Nguyen van Yen, O. Pannekoucke, and K. Schneider. *Handbook of Environmental Fluid Dynamics*, volume 2, chapter Multiscale methods: Fractals, self-similar random processes and wavelets. Taylor and Francis, 2011.
- [6] LONGUET-HIGGINS M. S. 1995 Parasitic capillary waves: a direct calculation. *J. Fluids Mech.* **301**, 79–107.
- [7] B. Miquel and N. Mordant. Nonstationary Wave Turbulence in an Elastic Plate. *Phys. Rev. Lett.*, **107**(3):034501, 2011.
- [8] D. Queiros-Conde. A diffusion equation to describe scale- and time-dependent dimensions of turbulent interfaces. *Proc. R. Soc. Lond. A*, **459**:3043, 2003.
- [9] RAPP, R. J. & MELVILLE, W. K. 1990 Laboratory measurements of deep-water breaking waves. *Philosophical Transactions of the Roy. Soc. Lond. A* **331**, 735–800.
- [10] K. Schneider and M. Farge and N. Kevlahan, *Woods Hole Mathematics, Perspectives in Mathematics and Physics*, volume 34, chapter Spatial intermittency in two-dimensional turbulence: a wavelet approach, pages 302–328. World Scientific, 2004.
- [11] SILVERMANN, B. W. & VASSILICOS, J. C. ed. 2000 Wavelets: the key to intermittent information. *Oxford University Press*.
- [12] L. Zhou, C. Rauh, and A. Delgado. *Synthetic Turbulence and Vortex Dynamics*, volume In Press of *Ercof-tac Series*, chapter Wavelet Multifractal Cascade Model and Synthetic Method for Fully Developed Turbulence. Springer, 1st edition, 2014.
- [13] with the standard definition  $i^2 = -1$
- [14] Actually it is 0.001, but the smallest time-scale which can be observed by the wavelet cannot be smaller than twice the lower cut-off scale.